Angular-dependent spin dynamics of a triad of permalloy macrospins

Wonbae Bang, F. Montoncello, M. B. Jungfleisch, A. Hoffmann, L. Giovannini, and J. B. Ketterson

Phys. Rev. B **99**, 014415 — Published 14 January 2019

DOI: 10.1103/PhysRevB.99.014415

Angular-dependent spin dynamics of a triad of permalloy macrospins

Wonbae Bang,[1,2*] F. Montoncello,[3] M. B. Jungfleisch,[2,4] A. Hoffmann,[2]
L. Giovannini,[3] and J. B. Ketterson[1,5]

[1] Department of Physics and Astronomy, Northwestern University, Evanston, IL 60208, USA
[2] Materials Science Division, Argonne National Laboratory, Argonne, IL 60439, USA
[3] Dipartimento di Fisica e Scienze della Terra, Università di Ferrara, Ferrara, ITALY
[4] Department of Physics and Astronomy, University of Delaware, Newark, DE 19716, USA
[5] Department of Electrical and Computer Engineering, Northwestern University, Evanston, IL 60208, USA

Abstract

We experimentally and theoretically characterize the angular dependent microwave response of three-macrospin-vertex structures that can serve as a node in various spin ice lattices. The macrospins consist of patterned permalloy thin films with an elliptical cross-section together with an in-plane aspect ratio allowing an Ising-like behavior together with bulk modes as low-frequency excitations in the field range of interest. Various branches of the frequency-magnetic field curves display atypical behaviors and discontinuities, together with softening due to macrospin reversals. The overall behavior observed accurately corresponds to a superposition of the spectra of the individual macrospins. The measured ferromagnetic resonance spectra are in good agreement with theoretical modeling. In particular, they reveal a close correlation between the field direction (relative to the individual macrospins), and the corresponding frequency-magnetic field curve; i.e., between the geometry and the magnetic response.

I. INTRODUCTION

There is currently much interest in artificial spin ice systems both as models for those occurring in crystalline solids as well as for their interest in the field of magnonics, where spin wave propagation promises to be a new means of low-power information delivery [1-8]. The magnetic responses of the artificial spin ice systems are largely controlled by various levels of magnetic frustration [8-10]. This arises from their highly degenerate ground states, imposed by a combination of: 1) competing magnetic dipole interactions at their nodes (where the macrospin links making up the lattice closely approach each other and where so-called ice rules apply [11]), and 2) the symmetry of the lattice itself [12, 13]. The static and dynamic response of spin ice lattices is generally rather complex [8, 10, 14], especially when complex magnetization distributions are concerned, arising from frustrated configurations or arbitrary magnetic field orientations [15, 16]. Li *et al*. [17, 18] reported

*Corresponding author.

Brillouin scattering measurements of spin wave modes in a square spin ice consisting of rectangular blocks for two different directions of the applied magnetic field and multiple thicknesses. However, their simulations were limited to the single and bi-elements elements making up the array. Yahagi *et. al.* [19] also utilized Brillouin spectra to observed spin wave modes from different sub-lattices, however metastable behavior arising from magnetization reversal, an important property, was not studied.

The present study aims at achieving a better understanding of the basic properties of interactions within individual spin-ice building blocks [20]. In particular, it would be of considerable interest to know to what extent the spectra of complex systems might be predicted from the specific spectrum of the individual irreducible [21] building blocks, a possibility strongly supported by the results presented here.

As a model building block, we here analyze the microwave dynamics of 120° symmetric kagome lattice vertex structures formed by three-macrospins, each having a uniform thickness and an elliptical cross section, using micromagnetic modeling and broad band ferromagnetic resonance (FMR) experiments. Each macrospin is fabricated as an elongated ellipse with major and minor axis of 500 and 200 nm, respectively, and a thickness of 15 nm. Since extremely elongated ellipses (which approximate ideal macrospins) are known to have low-frequency excitations localized in narrow regions at the ends of the structure [22, 23] (which give weak FMR signals), we chose the aspect ratio (5:2) as a compromise to achieve macrospin-like behavior but also low frequency excitations involving most of the dot surface ("bulk" modes). If periodically linked together, these vertices would form a kagome spin ice lattice system. In addition, we performed measurements and simulations on clusters, where one "macrospin" of the structure has a reduced width with an aspect ratio of 5:1 (a thinner macrospin) resulting in a larger shape anisotropy.

II. EXPERIMENTAL

The samples consist of a coplanar waveguide (CPW) on which a square array of well-separated three-macrospin (120°-symmetric) permalloy (Py: $Ni_{80}Fe_{20}$) kagome-vertex-like structures are patterned over the central strip, as shown in Fig. 1. This configuration involving metallic contact with the guide has been shown to achieve maximal coupling and sensitivity [24]. The CPWs and the macrospin vertex arrays were fabricated on Si substrates with a 300-nm SiO_2 layer using the following process. The conducting electrodes of the CPWs were formed with 5 nm of Ti covered by 100 nm of

Au that were patterned by optical lithography using a laser writer and electron beam evaporation followed by a lift-off process. The CPWs have a central line flanked by two ground lines, as shown schematically in Fig. 1. The central line has a 20-μm width, and there is an 8-μm spacing between this line and ground lines. The 15-nm thick Py three-macrospin vertex arrays were fabricated by electron beam lithography and electron beam evaporation, using a lift-off process. In order to have a reliable lift-off following metallization, a double layer of positive polymethyl methacrylate (PMMA) resist was applied using a spin-coater before electron beam lithography. The thicknesses of the Ti, Au, and Py films were monitored by a quartz crystal microbalance during the evaporation: deposition rates were ~0.2 Å/sec for Ti, ~1.4 Å/sec for Au, and ~0.4 Å/sec for Py, respectively, and the base pressure was ~3×10^{-7} Torr.

Figure 1 shows a schematic representation of a CPW together with a three-macrospin vertex array. In the apparatus used in these experiments, the external magnetic field (H) is constrained to lie along the guide axis, taken as the x-axis, and hence the microwave field (H_f) is largely along the y-axis; i.e., normal to H, which is the usual geometry in FMR experiments. In the sample shown in Fig. 1, the three-macrospin vertex is oriented at 0° relative to the guide axis. To explore the angular dependence, additional samples were prepared which are rotated by the angle θ = 15°, 30°, and 45° for the symmetric (aspect ratio = 5:2) samples and θ = 15°, 30°, 45°, 60°, 75°, and 90° for the asymmetric (aspect ratio = 5:1) samples.

In order to probe the dynamic response of the macrospin vertices, we performed broadband FMR measurements with a vector network analyzer (VNA) [25]. The VNA was connected via "picoprobes" to the CPW for recording the microwave absorption spectra, and the transmission parameter S_{21} was measured at a nominal microwave power of 0 dBm.

All spectra were recorded using the following routine: first, H was set at +3000 Oe, and the frequency swept between 2 and 10 GHz to establish a baseline which was subtracted from the data gathered at all other fields. Frequency sweeps were then carried out between 2 and 10 GHz for discrete H values ranging between +900 and –900 Oe. To establish the history dependence of the spectra, this procedure was repeated with H swept in the range –900 Oe to +900 Oe.

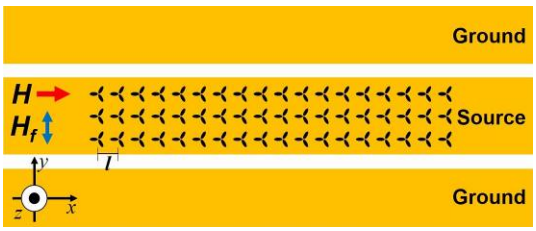

FIG. 1. Illustration of the 0° symmetric sample and measurement configuration. The permalloy three-macrospin vertex arrays are written on the central line of a CPW. The external magnetic field (H) is applied along the x-axis. An individual macrospin of the three-macrospin 120° symmetric vertex has dimensions of 500×200 nm^2 and a thickness of 15 nm. The square lattice has a spacing (l) of 1.88 μm.

III. THEORY AND SIMULATIONS

Theoretical calculations were performed using the dynamical matrix method (DMM) [26-28], which is based on both the solution of the Hamiltonian equations of motion for the spin precession and a micromagnetic representation of the magnetic system. In our case (non-interacting vertices), the sample consisted of a single vertex, made of three equivalent 15-nm thin cylinders with an elliptical cross section (500×200 nm^2), and was discretized with square-based elemental cells of $5 \times 5 \times 15$ nm^3. "A serrated edge" of the ellipses in the micromagnetic modelling, resulting from the square mesh, is known to weakly influence edge modes which are localized at the dot borders. However, such an influence is not expected for the bulk modes. The equilibrium configuration was calculated, for a given applied field angle and magnitude, by the Object Oriented MicroMagnetic Framework (OOMMF) software [29]. This equilibrium configuration was then entered into the software based on DMM, which outputs the corresponding eigenvalues (frequencies) and eigenvectors (profiles) that characterize the various spin wave modes. The magnetic parameters used were those for Py (saturation magnetization M_S = 700 kA/m, exchange stiffness constant A = 10 pJ/m).

IV. RESULTS AND DISCUSSION

A. Symmetric samples

Figure 2 shows scanning electron microscopy (SEM) images of the fabricated symmetric samples where all segments have the aspect ratio of 5:2 and 120° rotational symmetry together with a σ_v mirror symmetry. The individual macrospins have lateral dimensions of 500×200 nm^2 and are 15-nm thick. The spacing at the center, where the macrospins meet within a vertex, is about 100 nm. The vertex patterns are rotated by 15° between the different CPWs, and repeat on a square lattice with a lattice constant of 1.88 μm.

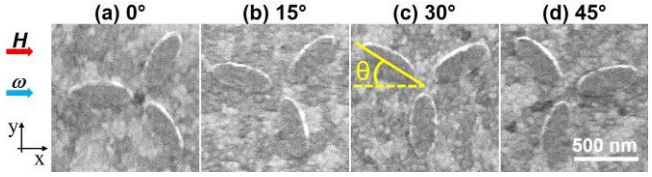

FIG. 2. SEM images of the four symmetric samples prepared. The lines indicate the angle (θ) between the static magnetic field direction and a major axis of one of the macrospins: ranging from θ = 0° (a) to 45° (d) in 15° steps.

Although beyond the scope of this paper, we briefly examine the general behavior of the magnetization with respect to both magnitude and direction of *H*. Due to the presence of the two vertex-partners the magnetization distribution is never exactly end-to-end symmetric, and the local magnetic charges [30-33] do not lie on a macrospin axes. An exception is when the field is parallel to a macrospin axis where it forms the symmetric "leaf state" (also referred to as an "onion state" in Ref. [34]) shown in Fig. 3(a). The magnetic configurations of each macrospin at any given field value determine the symmetry of the corresponding spin wave mode profiles, and, ultimately, the related frequency.

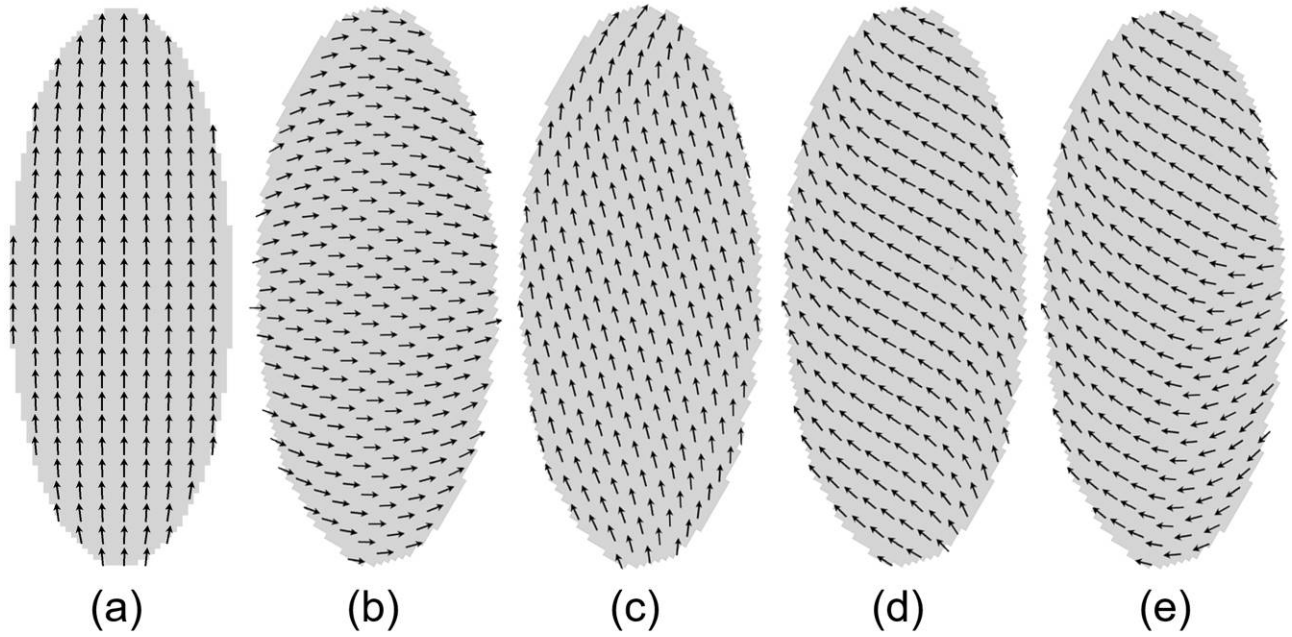

FIG. 3. Examples of calculated magnetization configurations at different fields for different ellipses in the vertex: (a) symmetric leaf state when the field is along the long axis; (b) leaf state when the field is along the short axis (slightly tilted); (c) and (d) two different S-state configurations, with asymmetries due to both the micromagnetic representation of an oblique ellipse, and the presence of other macrospins close to one end only, depending on the vertex geometry; (e) a metastable state lying between (b) and (c).

At specific negative *H* values, the reversals of the macrospins occur, in a sequence that depends on the specific symmetry of the system, determined by the angle θ. For the 0° symmetric sample shown in Fig. 2(a), the first critical field (H_{C1}) is –283 Oe where the two equivalent macrospins reverse. The second critical field (H_{C2}) is –415 Oe at which the macrospin lying parallel to *H* reverses.

At 15°, shown in Fig. 2(b), the macrospin oriented at 45° with respect to *H* switches at H_{C1} = –210 Oe; the calculations then show the joint reversal of the other two macrospins at H_{C2} = –230 Oe. At 30° in Fig. 2(c), we have two critical fields. The first, at H_{C1} = –230 Oe, occurs where the two equivalent macrospins, oriented at 30° to the external field direction, switch simultaneously. The second is associated with the ellipse having its long axis perpendicular to *H*, which starting from a "leaf state" (see Fig. 3(b)), undergoes the gradual rotation of the magnetization described above down to a field H_{C2} = –400 Oe (corresponding to a minimum in FMR frequency); the calculations exhibit intermediate metastable states in the range of –230 to –310 Oe, similar to that shown in Fig. 3(e). At 45° in Fig. 2(d), we have the single critical field H_{C1} = –250 Oe where two macrospins switch together, while the other macrospin initially undergoes a gradual magnetization rotation from a leaf state shown in Fig. 3(b) to an S-state shown in Fig. 3(c). Finally, at H_{C2} = –260 Oe, it switches to a reversed S-state shown in Fig. 3(d). The field range may be too narrow (ΔH = 10 Oe) to detect experimentally. For this reason, these intermediate calculated states must be considered speculative only, and a thorough study will be presented elsewhere.

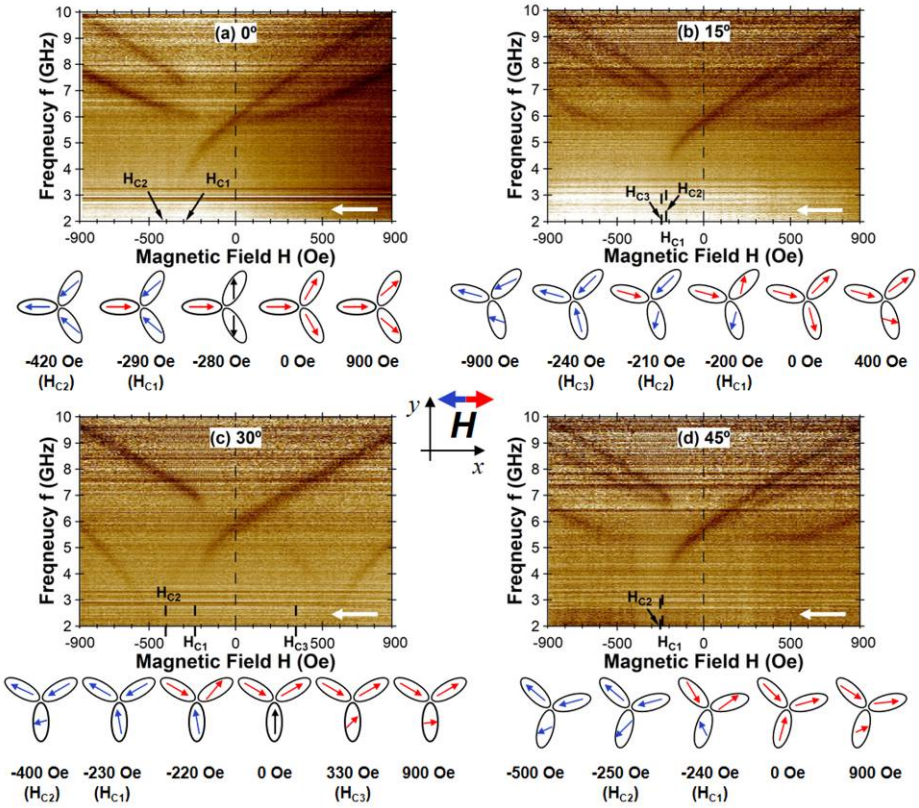

FIG. 4. Experimental FMR spectra together with simulated average macrospin orientations for the Py three-macrospin vertex arrays prepared with different angles (θ = 0° to 45° in 15° steps) between the magnetic field and a macrospin major axis. Here the frequency is swept between 2 and 10 GHz at fixed

magnetic fields ranging between +900 and –900 Oe. White arrows indicate the direction of the magnetic field changes during the measurement.

The FMR absorption spectra obtained with the VNA are shown as false color-coded images in Fig. 4. The simulated switching fields of the individual nano-ellipses in the cluster are also indicated in Fig. 4. An average orientation of the magnetization for each of the nano-ellipses is shown beneath the graphs. The frequency was swept from 2 to 10 GHz at a fixed H in the range +900 (after first saturating the samples at +3000 Oe) and –900 Oe. As seen in Fig. 4(a), two modes were clearly detected from the 0° symmetric sample. Note the higher lying mode exhibits a discontinuity on the negative H side at about –300 Oe. This change arises principally from a reversal of the direction of the magnetization of the principal ellipse that is aligned with the easy (long) axis, parallel (or anti-parallel) to the magnetic field [35]. The intensity of the lower frequency mode for the 0° sample shown in Fig. 4(a) is stronger than the higher frequency mode. In contrast, the intensity of the higher frequency mode for the 30°-sample shown in Fig. 4(c) is stronger than the lower frequency mode. Here the individual modes from the two rotated macrospins, which are slightly separated in the calculations shown Fig. 5(c-2) and (c-3) below, appear *superposed* in experiments.

In Fig. 4(c), the 30° sample shows a dramatic change for the lower frequency mode in comparison with the 0° sample. In particular, the frequency of this mode decreases as the field is reduced and disappears somewhat below 500 Oe followed by a new branch indicated by the black arrows in Fig. 4(c). This arises primarily from the macrospin with its long axis perpendicular to the H, which corresponds to the hard-axis [36].

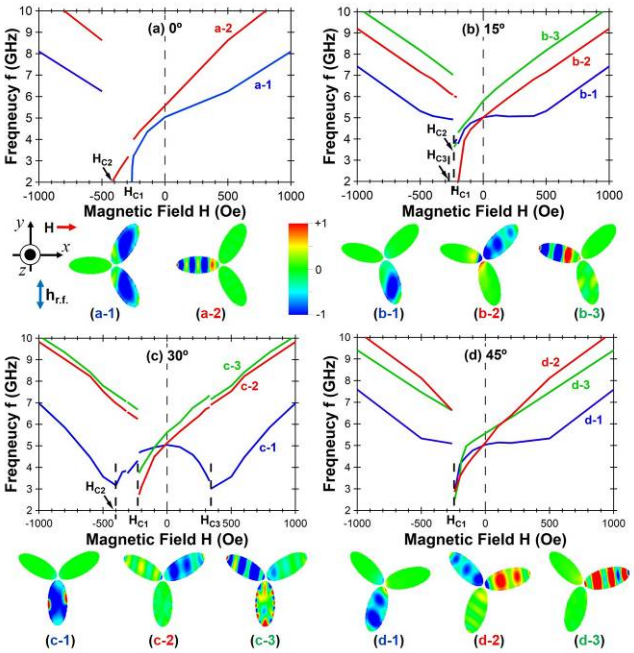

FIG. 5. Theoretical simulations of the frequency vs. magnetic field dispersions and the corresponding out-of-plane component of the magnetization at +1000 Oe for each mode for the four symmetric samples with different angles (θ = 0° to 45° in 15° steps).

We show the results of the calculations for the four orientations studied in the experiments in Fig. 5. As first found in Ref. [20], in separated macrospin vertices (i.e., interacting only magnetostatically), the modes that are likely to give a large FMR signal consist of the fundamental modes of each individual macrospin. In the present case, we might anticipate three main modes, each localized in one of the three macrospins. However, due to a combination of shape anisotropy and dipolar interdot interactions, these fundamental modes can occasionally show nodal lines rather than the ideal nodeless uniform Kittel mode of a macrospin. Moreover, in some cases, the localization to a single macrospin is not exact, and spurious oscillations appear in other macrospins (e.g., c-3 and d-2 in Fig. 5). Depending on the sample-to-*H* orientation (e.g., for symmetry reasons) different fundamental modes can occur at the same frequency thereby merging into a single mode profile, as in the case θ = 0° (e.g., branch a-1 in Fig. 5) where the measured FMR intensity [37] is particularly intense, as remarked above. When the three-macrospin vertex is tilted with respect to the x-axis, the magnetization of each of the three-macrospins is oriented differently with respect to the *H*, so their energies and individual fundamental mode frequencies differ, as can be seen at 15°, where we distinguish three curves, corresponding to three different modes. A larger angle between a macrospin easy axis and the *H* direction shows a lower corresponding fundamental mode frequency, because the demagnetizing field for that macrospin is larger [38].

The 30°-case deserves a more detailed discussion. At θ = 30°, the field *H* is perpendicular to the long axis of one of the three-macrospins, and at an angle of 30° with respect to the other two. Hence, we expect these two macrospins to have equivalent dynamics: their fundamental modes occur at the same frequency, which is lower than that of the inequivalent (perpendicular) macrospin. Accordingly, the fundamental modes of these two macrospins are calculated to lie very close in frequency, justifying the rather large FMR peak found in the experiments. In contrast, the lowest curve corresponds to the mode localized in the macrospin with its long axis perpendicular to *H*. As found and explained in Ref. [35], when *H* is decreased the frequency of its fundamental mode follows a typical "W-shape" curve (characteristic of an isolated ellipse), with two minima. In this case, the minima are centered at about H_{C2} = –400 Oe and H_{C3} = 340 Oe in the calculations in Fig. 5(c) and at about ±500 Oe in the experiment in Fig. 4(c) with a maximum near *H* = 0. In decreasing from high field values to H_{C3}, the magnetization of this macrospin is mainly oriented parallel to the short axis, i.e., a leaf state, as shown in Fig. 3(b). The magnetization begins to curl in an S-like fashion below H_{C3} [34, 35], as shown in Fig. 3(c) and (d) and rotate toward the other two macrospins, increasingly aligning to the long axis due to shape anisotropy; the consequence of this rotation is a frequency increase up to a maximum which occurs in the vicinity of *H* = 0. On passing through zero (or possibly at a negative field due the perturbation induced by the other two ellipses, which have not yet switched), the magnetization again begins to curl (now in the opposite sense) and rotate counterclockwise up to H_{C2} where the negative *H* minimum occurs, after which the curves are the exact images of positive *H* values. In calculations, slight discontinuities can be seen in approaching H_{C2} due to discretization errors. On the other hand, the other two modes follow a Zeeman-like behavior (i.e., the corresponding frequency curve is nearly linear with the applied field), progressively decreasing until, due to softening, the macrospins suddenly switch their magnetization at H_{C1} = –230 Oe.

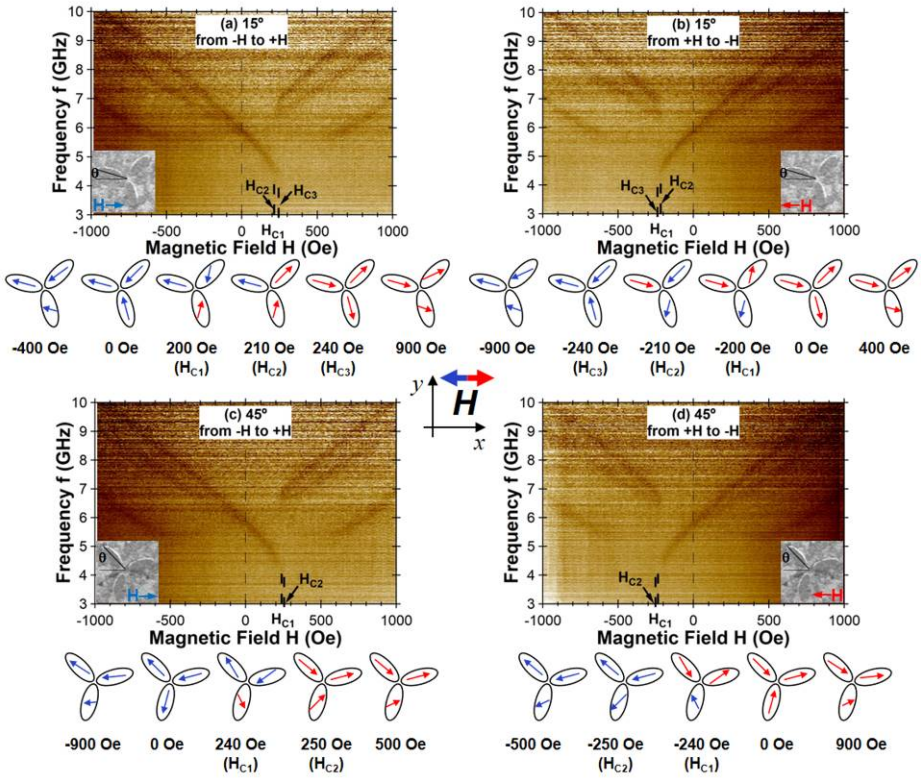

FIG. 6. Experimental FMR spectra under field reversal for the samples oriented at 15° and 45°. Also shown is an average macrospin orientation of the individual ellipses. The inset is an SEM image indicating the orientation of the vertex.

For the 15° and 45° samples, all three ellipses differ with respect to their alignment with H, and hence there are three principal frequencies, as shown in Fig. 4(b) and (d). Note that the spectrum of the 15° sample in Fig. 4(b) is essentially identical to that for 45° in Fig. 4(d). This behavior is expected for a system that is symmetric under the operation $H \rightarrow -H$. To test this point, we performed additional experiments shown in Fig. 6 in which H was swept in *both* directions. These H reversal experiments were carried out for both the 15° and 45° samples. Note the required global mirror symmetry between the results of the negative to positive field sweep at 15° and the positive to negative sweep at 45° (and likewise the positive to negative sweep at 15° and the negative to positive sweep at 45°). On the other hand, experimental field sweeps from positive to negative fields at 15° and 45°, which differ slightly in the simulations [see Fig. 5(b) and (d)], are also nearly identical.

B. Asymmetric samples

Figure 7 shows SEM images of the seven asymmetric samples fabricated. The axes of the ellipses are still oriented at 120° with respect to each other, however now one of the ellipses has lateral dimensions of 500 × 100 nm^2 while the remaining two continue to have lateral dimensions of 500 ×

200 nm^2. The thickness of the Py is the same at 15 nm. The spacing at the center among the macrospins making up one vertex is about 100 nm. The three-macrospin patterns are rotated by 15° between successive CPWs, and repeat on a square lattice with a lattice constant of 1.88 μm.

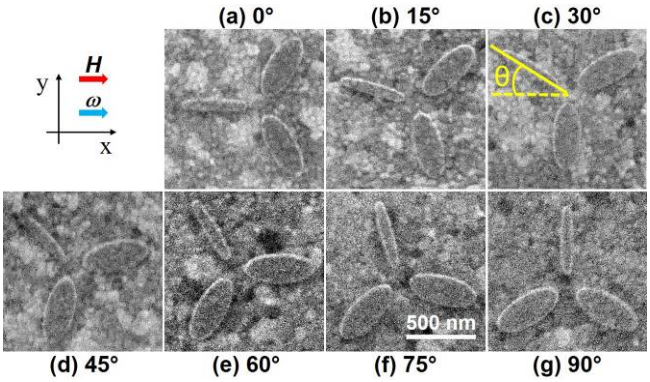

FIG. 7. SEM images of all seven asymmetric samples prepared. The lines in (c) indicate the angle (θ) between the magnetic field direction, and a major axis of the thinner macrospin: ranging from θ = 0° (a) to 90° (g) in 15° steps.

Figure 8 shows the FMR absorption spectrum of the asymmetric samples obtained with the same measurement setup as for the symmetric samples. Beneath the experimental spectra we show an average orientation of the magnetization for each of the nano-ellipses at a specific magnetic field. Overall, modes arising from the thinner macrospin were *not observed* for the asymmetric samples; their contribution is too small to provide sufficient power to be seen for the sensitivity at which these experiments were performed. In addition, changes of the dynamics of the other modes were not observed. Hence, this thinner macrospin serves as "defect", which when introduced in the vertex makes it asymmetric, but remains "hidden" in the FMR spectra and neutral (of little impact) with respect to the behavior of the frequencies of the remaining modes. This observation, together with conclusions about the symmetric vertex dynamics, supports the idea that the dominant (fundamental) modes of magnetostatically interacting Ising-like macrospins largely behave *independently of each other*. As a result, for this asymmetric vertex case, only two modes are observed for an arbitrary field direction.

Only a single mode is observed for 0° and 90° since *H* makes the *same angle* with respect to the two larger macrospins at these angles, and the dynamic magnetization in the two macrospins occurs at the same frequency by symmetry; note the related curve in Fig. 8(a) corresponds to the lower curve of Fig. 4(a). The spectra for the asymmetric case at the remaining angles θ = 15°, 30°, 45°, 60°, and 75°, can be seen to closely correspond to those for the symmetric case at θ = 15°, 30°, 15°, 0°, and 15° *provided* the contribution of one of the elliptical macrospins (that corresponding to the thinner one) is removed.

At θ = 30° in Fig. 8(c), a mode, which is indicated by an arrow in the negative field side, is slightly shifted towards higher field and higher frequency side compared to theoretical simulation in Fig. 9(c).

In Fig. 9, we show the calculated curves for the asymmetric samples. The agreement with the experiments is very good and justifies the interpretation given above. We remark that the major discontinuities in the frequency curves correspond to the macrospin reversals, while the small discontinuities (and occasionally irregular curve branches) likely arise from issues of numerical accuracy. Interestingly, H_{C1}, which is relevant to the two larger macrospins, is about the same (between –190 and –250 Oe) independent of the θ. In contrast, H_{C2} (relevant to the thin macrospin) has a minimum (–500 Oe) at θ = 30°, tending toward infinity at θ = 90°, where reversal is attained by a gradual rotation of the magnetization without discontinuities.

In addition to the FMR-active modes, calculations show the existence and behavior of the fundamental mode of the thinner macrospin (dashed lines in Fig. 9), which is not detected in the experiments. Due to the larger shape anisotropy, the magnetization of this macrospin switches with a discontinuity which is the largest at θ = 0°, and zero (no discontinuity) at θ = 90°. In fact, at 90° the magnetic moments, initially tilted more than 45° with respect to the *H*, gradually rotate with decreasing field under the influence of the shape anisotropy fields (see refs. [23, 35]). The discontinuity and continuity of the magnetization reflects a similar discontinuity and continuity in the frequency of the fundamental mode. When the magnetization is aligned to the easy axis, the switching field in the negative *H* side is the largest at 0°, whereas reversal is attained through a gradual rotation at θ = 90°.

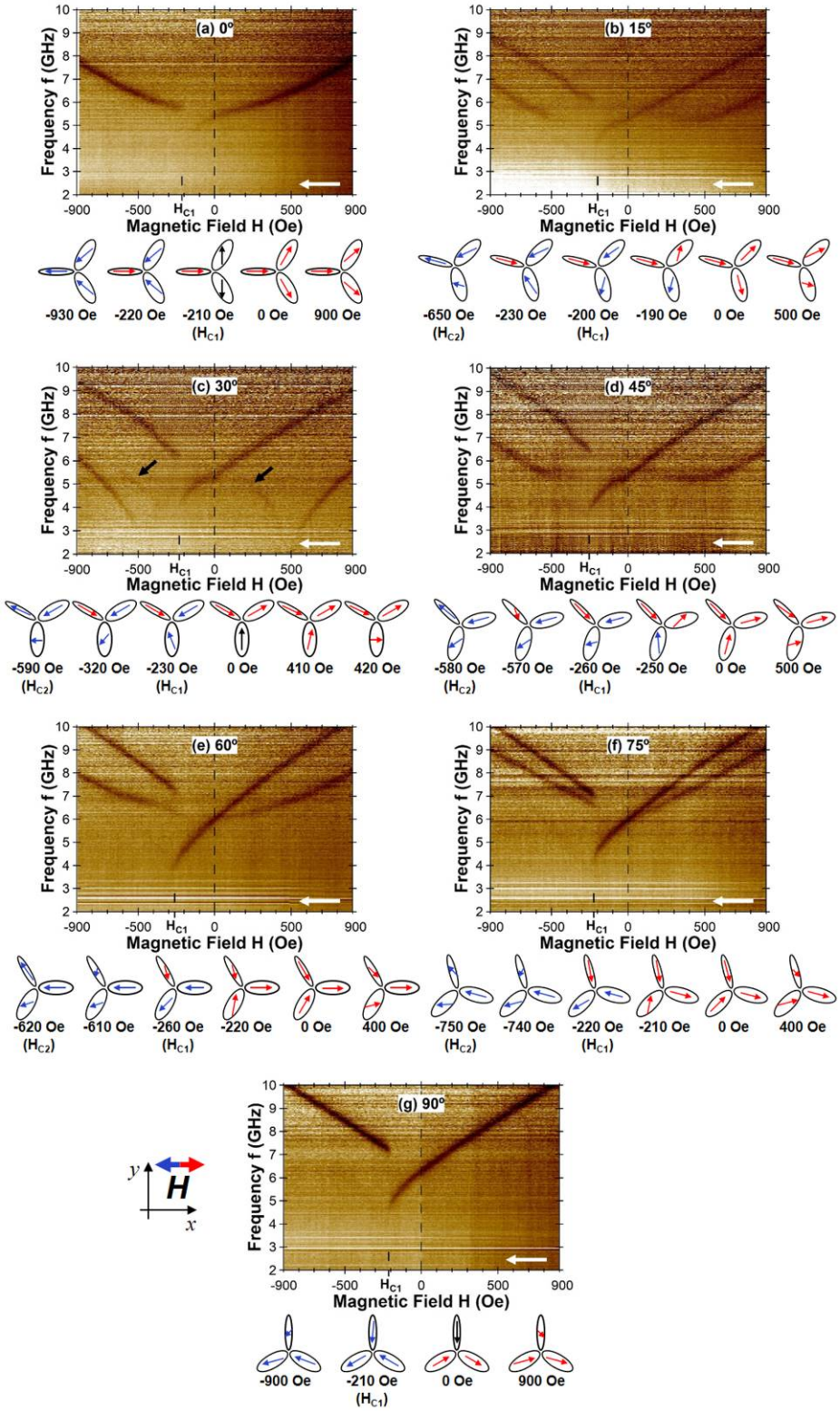

FIG. 8. Experimental FMR spectra and simulated average macrospin orientations obtained for the seven asymmetric samples consisting of Py three-macrospin-vertex arrays prepared with different angles from θ = 0° to 90° between the magnetic field and the thinner macrospin major axis. Here the frequency is swept between 2 and 10 GHz at fixed magnetic fields ranging between +900 and –900 Oe. White arrows indicate the direction of the magnetic field sweep.

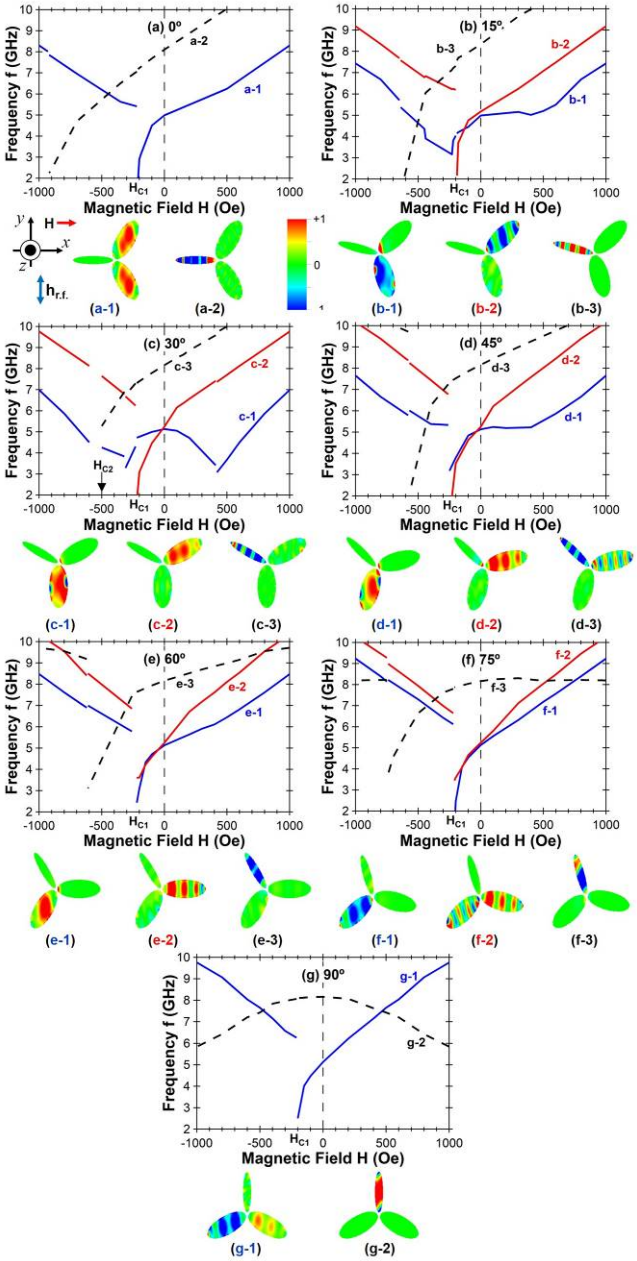

FIG. 9. Theoretical simulations of the frequency vs. magnetic field behavior together with the corresponding out-of-plane component of the magnetization at +1000 Oe for each mode of the seven asymmetric samples with different angles ($\theta = 0°$ to 90° in 15° steps). Dashed lines correspond to the fundamental mode confined to the thinner macrospin.

Remarkably, the frequency of this macrospin mode is clearly tunable over a wide range at positive H, determined by the possible different H orientations, and this range progressively increases with increasing field (Fig. 10). As an overall description of this feature, we observe that the slope of the $\omega(H)$ curves for the thin macrospin mode can be regarded as an "effective macrospin gyromagnetic

ratio", $\gamma_{eff} = d\omega/dH$, which can be tuned from positive to zero or even negative simply by changing the H angle. This effective quantity, which, in principle, could be obtained through *dynamic* FMR measurements, provides information on the *static* distribution of the magnetic moments in this macrospin and their evolution, from high fields down to zero, as shown in Fig. 10. The maximum of γ_{eff} arises when the magnetization is parallel to the long axis (i.e., when $\theta = 0°$); γ_{eff} decreases with increasing θ, because the starting magnetization is increasingly misaligned from the easy axis, and a progressive rotation towards the easy axis occurs for decreasing H. This rotation is a rearrangement of magnetic moments, implying a change of dipolar and exchange contributions to the spin wave frequency; the maximum effect is seen at $\theta = 90°$, when γ_{eff} assumes the largest negative value. In this latter case, the initial magnetization is not parallel to the field (hence, is not perpendicular to the macrospin) but tilted, because of both the large shape anisotropy of the thin macrospin and the dipolar fields of the other vertex macrospins; as a consequence, the magnetization reversal involves a rotation angle less than 180°. Note that, in fact, only the magnetization component is parallel to the field direction is reversed.

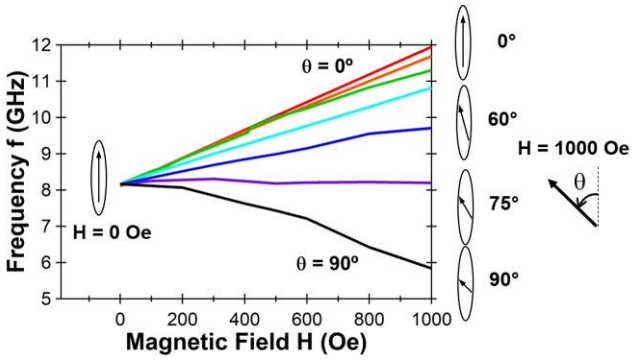

FIG. 10. Frequency vs. magnetic field curves in the range of 0 to 1000 Oe at varied angles between 0° to 90° in 15° steps for the fundamental mode of the thin macrospin; only the positive field part is shown and the behavior is relatively linear. At each field value, the ultimate frequency can be tuned over a wide range (6 GHz at 1000 Oe), depending on the applied field direction. The inset is a schematic of an average orientation of magnetization at initial field (1000 Oe) and final field (0 Oe).

Finally, since this reversal occurs through a gradual rotation, without discontinuities, the $\omega(H)$ curve of the thin macrospin mode has the typical continuous W-shape discussed above and in Refs. [23, 35]. Of course, apart from numerical and discretization errors, the mode frequency at $H = 0$ is almost the same, independent of the orientation angle θ (as occurs when the magnetization is aligned with the major macrospin axis). In principle, from the angular and field dependence of γ_{eff} one can identify contributions from particular elongated macrospins in other systems and utilize it to interpret their

overall behavior. Based on such an understanding, one can speculate that it could be useful for a deterministic frequency modulation of spin waves carrying information in macrospin networks.

5. CONCLUSIONS

In conclusion, the above study, apart from its intrinsic interest, has strong implications with regard to artificial spin ice studies involving lattices formed from clusters of the type examined. Unlike previous reports [17-20], what our study demonstrates is that the spectra of lattices involving weakly coupled clusters of individual macrospins may be viewed as a *superposition* of the spectra of those macrospins. Using this *additivity principle,* intensity measurements could then yield the *fraction* of the individual macrospins presenting *different angles* with respect to the external magnetic field. Furthermore, the contribution to the overall spectrum from chosen macrospins can be largely suppressed by reducing their width, a tool that could be exploited in examining more complex structures.

ACKNOWLEDGEMENTS

Work at Northwestern was supported under NSF grant DMR 1507058. Device fabrication was carried out at Argonne and supported by the U.S. Department of Energy, Office of Science, Materials Science and Engineering Division. Lithography was carried out at the Center for Nanoscale Materials, an Office of Science user facility, which is supported by DOE, Office of Science, Basic Energy Science under Contract No. DE-AC02-06CH11357.

REFERENCES

[1] G. Gubbiotti, L. L. Xiong, F. Montoncello, and A. O. Adeyeye, Appl. Phys. Lett. **111**, 192403 (2017).

[2] J. Stigloher, M. Decker, H. S. Korner, K. Tanabe, T. Moriyama, T. Taniguchi, H. Hata, M. Madami, G. Gubbiotti, K. Kobayashi, T. Ono, and C. H. Back, Phys. Rev. Lett. **117**, 037204 (2016).

[3] A. V. Chumak, A. A. Serga, and B. Hillebrands, J. Phys. D **50**, 244001 (2017).

[4] A. V. Chumak, V. I. Vasyuchka, A. A. Serga, and B. Hillebrands, Nat. Phys. **11**, 453 (2015).

[5] J. Drisko, T. Marsh, and J. Cumings, Nat. Commun. **8**, 14009 (2017).

[6] A. Farhan, P. M. Derlet, L. Anghinolfi, A. Kleibert, and L. J. Heyderman, Phys. Rev. B **96**, 064409 (2017).

[7] V. V. Kruglyak, S. O. Demokritov, and D. Grundler, J. Phys. D **43**, 264001 (2010).

[8] C. Nisoli, R. Moessner, and P. Schiffer, Rev. Mod. Phys. **85**, 1473 (2013).

[9] E. Mengotti, L. J. Heyderman, A. F. Rodriguez, F. Nolting, R. V. Hugli, and H. B. Braun, Nat. Phys. **7**, 68 (2011).

[10] R. F. Wang, C. Nisoli, R. S. Freitas, J. Li, W. McConville, B. J. Cooley, M. S. Lund, N. Samarth, C. Leighton, V. H. Crespi, and P. Schiffer, Nature **439**, 303 (2006).

[11] Y. Qi, T. Brintlinger, and J. Cumings, Phys. Rev. B **77**, 094418 (2008).

[12] W. R. Branford, S. Ladak, D. E. Read, K. Zeissler, and L. F. Cohen, Science **335**, 1597 (2012).

[13] Y. C. Shen, O. Petrova, P. Mellado, S. Daunheimer, J. Cumings, and O. Tchernyshyov, New J. Phys. **14**, 035022 (2012)

[14] V. S. Bhat, J. Sklenar, B. Farmer, J. Woods, J. T. Hastings, S. J. Lee, J. B. Ketterson, and L. E. De Long, Phys. Rev. Lett. **111**, 077201 (2013).

[15] D. M. Burn, M. Chadha, and W. R. Branford, Phys. Rev. B **92**, 214425 (2015).

[16] E. Iacocca, S. Gliga, R. L. Stamps, and O. Heinonen, Phys. Rev. B **93**, 134420 (2016).

[17] Y. Li, G. Gubbiotti, F. Casoli, F. J. T. Goncalves, S. A. Morley, M. C. Rosamond, E. H. Linfield, C. H. Marrows, S. McVitie, and R. L. Stamps, J. Phys. D **50**, 015003 (2017).

[18] Y. Li, G. Gubbiotti, F. Casoli, S. A. Morley, F. J. T. Goncalves, M. C. Rosamond, E. H. Linfield, C. H. Marrows, S. McVitie, and R. L. Stamps, J. Appl. Phys. **121**, 103903 (2017).

[19] Y. Yahagi, C. R. Berk, B. D. Harteneck, S. D. Cabrini, and H. Schmidt, Appl. Phys. Lett. **104**, 162406 (2014).

[20] F. Montoncello, L. Giovannini, W. Bang, J. B. Ketterson, M. B. Jungfleisch, A. Hoffmann, B. W. Farmer, and L. E. De Long, Phys. Rev. B **97**, 014421 (2018).

[21] Namely, in a network, it is possible to identify a reduced number of macrospins, each one representing a class having a given geometry/magnetization (i.e., symmetry) with respect to the applied field.

[22] S. O. Demokritov, B. Hillebrands, and A. N. Slavin, Phys. Rep. **348**, 441 (2001).

[23] G. Gubbiotti, G. Carlotti, T. Okuno, M. Grimsditch, L. Giovannini, F. Montoncello, and F. Nizzoli, Phys. Rev. B **72**, 184419 (2005).

[24] M. B. Jungfleisch, W. Zhang, E. Iacocca, J. Sklenar, J. Ding, W. Jiang, S. Zhang, J. E. Pearson, V. Novosad, J. B. Ketterson, O. Heinonen, and A. Hoffmann, Phys. Rev. B **93**, 101401(R) (2016).

[25] S. S. Kalarickal, P. Krivosik, M. Z. Wu, C. E. Patton, M. L. Schneider, P. Kabos, T. J. Silva, and J. P. Nibarger, J. Appl. Phys. **99**, 093909 (2006).

[26] L. Giovannini, F. Montoncello, and F. Nizzoli, Phys. Rev. B **75**, 024416 (2007).

[27] M. Grimsditch, L. Giovannini, F. Montoncello, F. Nizzoli, G. K. Leaf, and H. G. Kaper, Phys. Rev. B **70**, 054409 (2004).

[28] K. Rivkin, A. Heifetz, P. R. Sievert, and J. B. Ketterson, Phys. Rev. B **70**, 184410 (2004).

[29] M. J. Donahue and D. G. Porter, "OOMMF User's Guide, Version 1.0," NISTIR 6376 (1999).

[30] D. Goll, G. Schutz, and H. Kronmuller, Phys. Rev. B **67**, 094414 (2003).

[31] G. Gubbiotti, L. Albini, G. Carlotti, M. De Crescenzi, E. Di Fabrizio, A. Gerardino, O. Donzelli, F. Nizzoli, H. Koo, and R. D. Gomez, J. Appl. Phys. **87**, 5633 (2000).

[32] P. Mellado, O. Petrova, Y. C. Shen, and O. Tchernyshyov, Phys. Rev. Lett. **105**, 187206 (2010).

[33] J. P. Park, P. Eames, D. M. Engebretson, J. Berezovsky, and P. A. Crowell, Phys. Rev. Lett. **89**, 277201 (2002).

[34] J. K. Ha, R. Hertel, and J. Kirschner, Phys. Rev. B **67**, 064418 (2003).

[35] F. Montoncello, L. Giovannini, F. Nizzoli, P. Vavassori, M. Grimsditch, T. Ono, G. Gubbiotti, S. Tacchi, and G. Carlotti, Phys. Rev. B **76**, 024426 (2007).

[36] W. Bang, F. Montoncello, M. B. Jungfleisch, A. Hoffmann, L. Giovannini, and J. B. Ketterson, (unpublished).

[37] We recall here that the theoretical mode power (i.e., strength) is the square modulus of the integral, over the whole particle surface, of the out-of-plane dynamic magnetization. The more the node number, the little the power; the larger the localization area, the larger the power.

[38] C. Kittel, Phys Rev **73** (2), 155-161 (1948).